High sensitivity all-fiber bend sensor based on modal interferences in a ring core fiber

Fan Zhang (张 帆), Beibei Qi (齐贝贝), Baijin Su (苏柏缙), Ou Xu (许 鸥)*, and Yuwen Qin (秦玉文)

Institute of Advanced Photonics Technology, School of Information Engineering, and Guangdong Provincial Key Laboratory of Information Photonics Technology, Guangdong University of Technology, Guangzhou 510006, China

We proposed and experimentally demonstrated an all-fiber sensor for measuring bend with high sensitivity based on a ring core fiber (RCF) modal interferometer. The sensor was fabricated by splicing a segment of RCF between two pieces of multimode fiber (MMF) and single-mode fiber (SMF) at the ends of the MMF as lead-in and lead-out. Due to the first segment of the MMF, the transmitted light is coupled into the ring core, silica center, and cladding of the RCF, exciting multiple modes in the RCF. By the modal interferences in the structure, bending sensing can be realized by interrogating the intensity of the interference dip. Experimental results show a high bending sensitivity of $-25.63\,\mathrm{dB/m^{-1}}$ in the range of $1.0954\,\mathrm{m^{-1}}$ to $1.4696\,\mathrm{m^{-1}}$. In addition, the advantages of the bend sensor, such as small size, low temperature sensitivity, and simple fabrication process, can be used for curvature measurement in building health monitoring.

Keywords: optical fiber sensor; curvature; temperature; ring core fiber.
DOI: 10.3788/COL202321.051201

1. Introduction

Optical fiber sensors (OFSs) have been widely investigated in various measurements, for instance, temperature[1], humidity[2], refractive index[3], strain[4], curvature[5], liquid level[6], and torsion[7,8]. Bending measurement plays a significant role in robotics applications, structural health monitoring, etc. Different types of optical fiber bend sensors have been reported, based on devices such as fiber Bragg gratings (FBGs), long-period fiber gratings (LPFGs), Mach–Zehnder interferometers (MZIs), Fabry–Perot interferometers (FPIs), Michelson interferometers (MIs), and multimode interferometers (MMIs).

The development of optical fiber sensors closely depends on optical fiber manufacturing technology. In recent years, the unique ring core fiber (RCF) with ring refractive index layer, is designed for mode-division multiplexing (MDM) and orbital angular momentum (OAM) transmission[9]. In 2019, Xuan et al. reported a microfiber MZI based on RCF and measured the temperature and refractive index[10]. The experimental results show that the temperature and refractive index sensitivities are around 64 pm/°C and 44 nm/RIU, respectively. Similarly, Yu et al. proposed a high-sensitivity microfiber MZI temperature sensor[11]. The sensor was fabricated by heating and stretching an RCF with the hydrogen flame. The sensitivity is 186.6 pm/°C when the cladding diameter of RCF is 72.58 µm. In 2021, Wei et al. proposed a sensor for simultaneous measurement of temperature and curvature by the RCF[12]. At the same time, they reported

an RCF MZI with dual demodulation of temperature and refractive index[13]. In 2022, Dong et al. reported an optical curvature sensor with a high resolution based on an in-line fiber MZI and microwave photonic filter[14]. Bai et al. proposed a curvature sensor, which is fabricated by splicing a segment of RCF between two pieces of single-mode fibers (SMFs) with two up-tapers[15]. Our previous works proposed an MZI curvature sensor based on the SMF–RCF–SMF structure[5]. The sensor was fabricated by splicing a segment of RCF between two pieces of SMF. The curvature measurement can be achieved by monitoring wavelength shifts of the interference dip. The experimental results show that the curvature sensitivity is $-4.370\,\mathrm{nm/m^{-1}}$, within the range of $1.199–1.549\,\mathrm{m^{-1}}$.

The above reported sensors are mainly based on wavelength interrogation. In addition to wavelength interrogation, intensity interrogation can be used to achieve sensing measurements. Dong et al. proposed an intensity-modulated fiber sensor for bending measurement[16]. Zhang et al. fabricated a bending sensor based on fiber-optic spindle arrays[17]. Bend sensing for intensity interrogation was achieved using an SMF spiral structure by He et al.[18]. Marrujo-Garcia et al. reported a temperature-independent curvature sensor based on in-fiber MZI using hollow-core fiber[19]. The curvature sensitivity of the proposed sensor reached $-17.28 \pm 2.3\,\mathrm{dB/m^{-1}}$.

This paper proposed and experimentally demonstrated a high sensitivity bend sensor using modal interferences and intensity

interrogation. The sensor was fabricated by splicing a segment of RCF between two pieces of multimode fibers (MMFs), forming an MMF–RCF–MMF (MRM) structure. Then the structure of MRM is sandwiched between the lead-in and lead-out SMFs. Due to the mode mismatch, multiple modes are excited in the RCF. Results show that the average bend sensitivity for intensity is $-25.63\,\mathrm{dB/m^{-1}}$ in the range 1.0954–$1.4696\,\mathrm{m^{-1}}$, by monitoring the intensity of interference dip (at 1450 nm). The proposed sensor has the advantages of high sensitivity, small size, and simple fabrication.

2. Sensor Principle

The schematic diagram of the proposed sensor is illustrated in Fig. 1(a). First, the lead-in SMF is spliced with the MMF by the automatic splicing mode of the fusion splicer (Atomo WAVE SFS-A63), and then the MMF is cut to the selected length. Second, the lead-out SMF and MMF are spliced and cut in the same way. Finally, a 10 mm long RCF is fused between the two MMF sections in a cladding-aligned manner. The RCF is composed of a ring core, a silica center, and outer cladding, the cross-sectional microscopic view of which is shown in Fig. 1(b).

The ring core, silica center, and cladding diameters are 15.14, 7.38, and 125 µm, respectively. The core and cladding refractive indices of RCF are 1.4728 and 1.4597, separately. The core and cladding diameters of the MMFs are 105 and 125 µm, respectively, a cross-sectional microscopic view of which is shown in Fig. 1(c). The core diameter, cladding diameter, and mode field diameter (MFD) of the SMF are 9, 125, and 10.2 µm, respectively.

In the proposed scheme, the MMFs play the role of a coupler for splitting and coupling. At the same time, to avoid phase differences between different modes in the MMF, the lengths of the MMF are limited to no more than 1 mm[20]. Considering the possibility of fusion and the compactness of the structure, the length of the RCF is set to 10 mm. To understand the effect of the MMF in the structure, the propagation field distribution is simulated by the beam propagation method. Figure 2(a) displays the light transmission in the SMF–RCF–SMF (SRS) structure. It can be seen that the energy is mainly distributed in the ring core and silica center, and the cladding only has weak leakage energy. In Figs. 2(b) and 2(c), simulation results of the SMF–MMF–RCF–SMF (SMRS) and SMF–MMF–RCF–MMF–SMF (SMRMS) structures are shown, respectively. Compared with
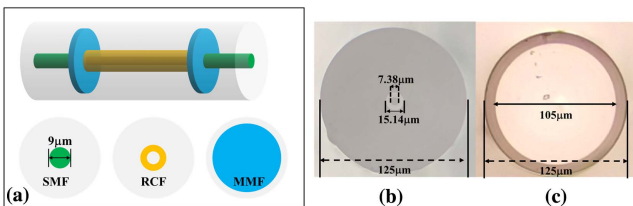

Fig. 1. (a) Schematic of the proposed sensor. Cross-sectional microscope view of (b) RCF and (c) MMF.
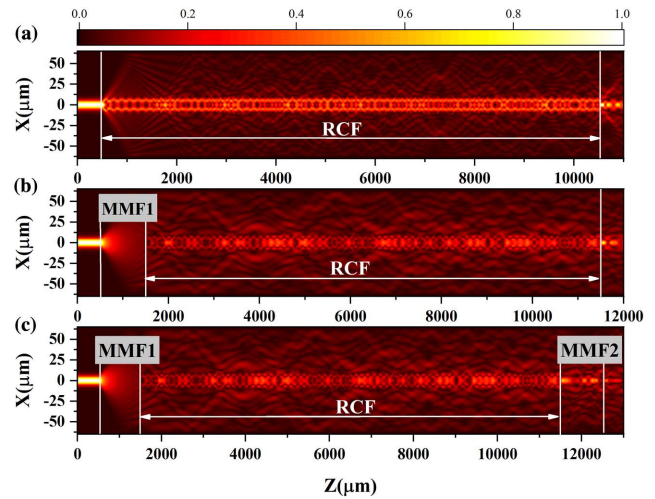

Fig. 2. Propagation field distribution with different structures. (a) SMF–RCF–SMF; (b) SMF–MMF–RCF–SMF; and (c) SMF–MMF–RCF–MMF–SMF.

the SRS, the energy in the RCF cladding is significantly enhanced for the SMRS and SMRMS structures. And the SMRMS recouples light from the RCF to the lead-out SMF with high efficiency due to the second segment of the MMF. The incident light from the SMF will first be coupled and expanded in the MMF1. Then this expanded beam is split and enters the RCF, exciting multiple modes in the RCF. Since these modes have different refractive index values, the optical path differences will be produced between any two of them. As a result, when these modes are recoupled into MMF2, modal interferences are formed.

The interference spectrum dips will locate at

$$\lambda_m = \frac{2\pi \cdot \Delta n_{\mathrm{eff}} L}{2m+1}, \qquad (1)$$

where Δn_{eff} represents the refractive index difference between different modes in the RCF, and λ_m represents the wavelength of the interference dip. From Eq. (1), the free spectral ranges (FSRs) can be written as

$$\mathrm{FSR} = \frac{\lambda_m^2}{\Delta n_{\mathrm{eff}} L}. \qquad (2)$$

Fiber bending causes strain change and disturbs the refractive index distribution of the cross section, which will lead to the deformation of mode fields. In Fig. 3, the refractive index distributions of the straight (blue curve) and bent (red curve) fibers are plotted, and it is evident that the bending causes a redistribution of the refractive index in the fiber. It means the effective refractive index of the ring core mode, silica center mode, and cladding mode will be changed. The mode field changes also induce energy redistribution among the ring core, silica center, and cladding areas, leading to alterations of interference fringes. The inset of Fig. 3 shows the simulation results of the light field distribution of the straight and bending fibers at $Z = 6500\,\mu\mathrm{m}$
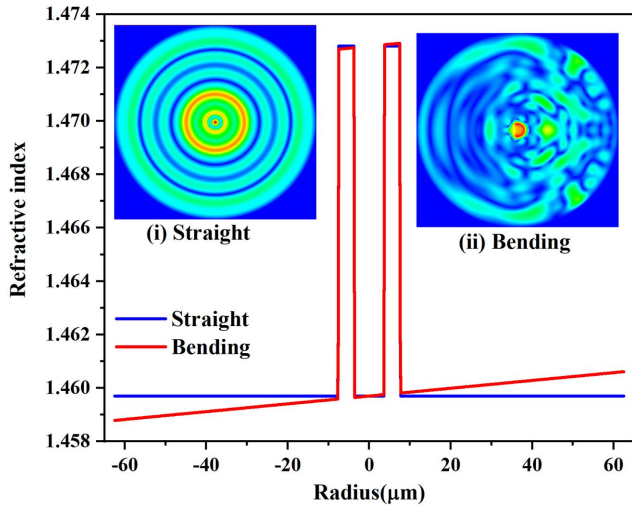
Fig. 3. Schematic diagram of the refractive index distribution of straight and bending fibers. The inset shows simulation results of the light field distribution at $Z = 6500$ µm.

[Fig. 2(c)]. It can be found that the bending obviously leads to the energy change in the RCF x–y section.

The transmission spectrum of the proposed sensor based on the SMRMS structure is displayed in Fig. 4(a). The FSR and
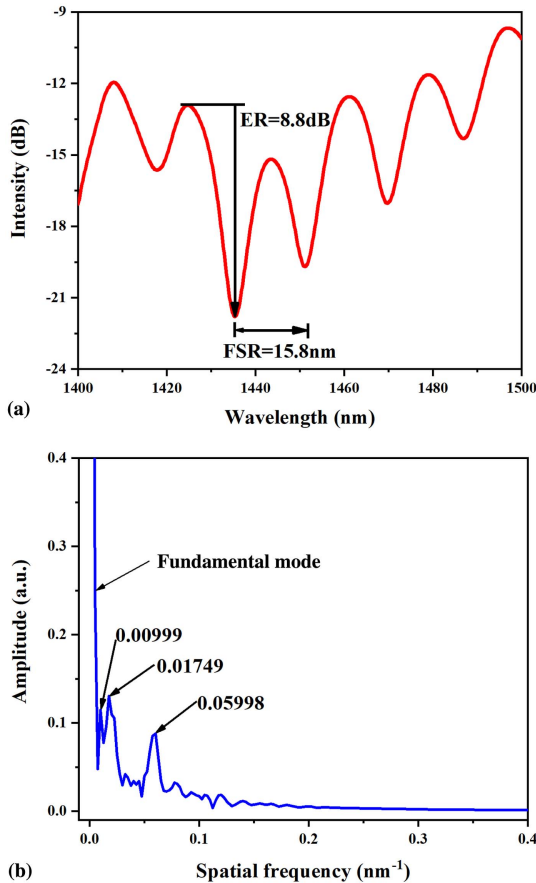

Fig. 4. (a) Measured transmission spectrum; (b) FFT of measured spectrum.

extinction ratio (ER) are 15.8 nm and 8.8 dB. Figure 4(b) shows the spatial frequency spectrum of the transmission by fast Fourier transform (FFT). The multiple peaks in the spatial frequency spectrum verify that multiple modes are excited and participate in the interference. The dominant peak at zero corresponds to the fundamental mode. The frequencies of the three main peaks except the fundamental mode are $0.00999 \, \text{nm}^{-1}$, $0.01749 \, \text{nm}^{-1}$, and $0.05998 \, \text{nm}^{-1}$, respectively. The spatial frequency ζ is as follows:

$$\zeta = \frac{\Delta n_{\text{eff}} L}{\lambda^2}, \tag{3}$$

where λ is the center wavelength of the light source.

By transforming Eq. (3), the refractive index difference can be written as

$$\Delta n_{\text{eff}} = \frac{\zeta \lambda^2}{L}. \tag{4}$$

First, the refractive index of the RCF fundamental mode was calculated using the finite element method (FEM) to be 1.4685. Then, according to Eq. (4), the effective refractive index differences between the three main peaks and the fundamental mode are calculated as 0.0021, 0.0036, and 0.0126. They correspond to the core mode (LP$_{21}$ and LP$_{31}$) and higher-order cladding mode (LP$_{29}$) as shown in Fig. 5, respectively. The relative errors of the effective refractive index difference between the FEM simulation and those calculated by Eq. (4) are 0.03%, 0.11%, and 0.0004%, respectively. The interference spectrum is formed by the superposition of multiple interferences, which is the reason for the irregularity of the interference spectrum.

3. Experiment and Discussion

Figure 6 is a schematic diagram of the bend sensing system. A broadband source (BBS) with a range from 1250 to 1650 nm is the light source. An optical spectrum analyzer (OSA, Yokogawa, AQ6370D) is used to monitor changes in the transmission spectrum of the sensor. The sensor is fixed on a pair of 3D translation stages with an initial distance of L_0. By controlling the distance between two 3D translation stages, different bends can be applied to the sensor. The curvature can be calculated using
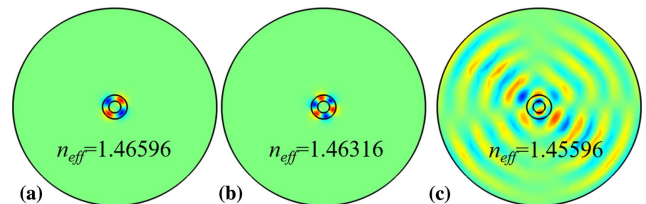

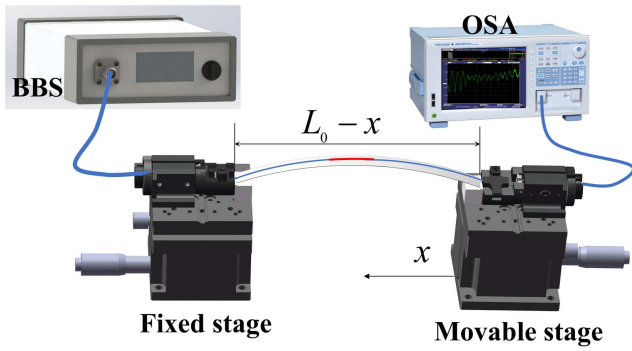**Fig. 5.** Mode field distribution are obtained by using FEM. (a) LP$_{21}$; (b) LP$_{31}$; (c) LP$_{29}$.

Fig. 6. Experimental setup for the curvature measurement.

$$C \approx \sqrt{\frac{24x}{L_0^3}}, \tag{5}$$

where C is the curvature, x is the displacement distance of the translation stage, and L_0 is the initial distance between two stages. In this experiment, $L_0 = 171$ mm.

The resonance dip around 1450 nm is chosen to indicate the bending-induced change in the transmission spectrum, as shown in Fig. 7(a). It can be found that the dip wavelength shifts to a longer wavelength with the curvature increase, and the intensity decreases with the curvature increase. The relationship between the average wavelength drift and bending for the four measurements are shown in Fig. 7(b). The inset shows the linear fitting of four testing results. The maximum wavelength curvature sensitivity is 1.67 nm/m^{-1}. The average wavelength curvature sensitivity is 1.64 nm/m^{-1}, and the R-square value is 0.99. Figure 8 shows the relationship between the average intensity variety of the four testing results and bend change. The inset shows the intensity-bending linear fitting results for four bending measurements. When the curvature is increased, the intensity shifts to the lower intensity direction. In the range of 0.4898–1.0954 m^{-1}, the maximum intensity-bending sensitivity is -12.73 dB/m^{-1}, and the R-square value is 0.97. Meanwhile, the maximum intensity-bending sensitivity up to the -25.53 dB/m^{-1} and R-square value of 0.98 are in the range from 1.0954 m^{-1} to 1.4696 m^{-1}. The average intensity-bending sensitivities for the four testing results are -11.35 dB/m^{-1} and

Fig. 8. Average intensity-bending response with error bars for four testing results; the inset shows the linear fitting of the four measurements.

-25.63 dB/m^{-1}, with a range of 0.4898–1.0954 m^{-1} and 1.0954–1.4696 m^{-1}, respectively.

The results of the four measurements according to Figs. 7(b) and 8 show that the sensor has good repeatability. For wavelength shift, the maximum standard deviation of the four measurements is 0.05 nm, which corresponds to a bending error of 0.03 m^{-1} with a sensitivity of 1.64 nm/m^{-1}. The maximum standard deviation of 0.4 dB for the intensity demodulation occurs in the range of 0.4898 m^{-1} to 1.0954 m^{-1}, where the resulting bending error is 0.03 m^{-1}.

Finally, the temperature responses of the sensor are also measured, and the results are displayed in Fig. 9, with temperature increasing from 30°C to 70°C. Based on Fig. 9(a), it can be found that the dip wavelength shifts to a longer wavelength as the temperature increases. The wavelength sensitivity of temperature is 64 pm/°C with an R-square value of 0.97. The maximum temperature sensitivity is 0.096 dB/°C at a temperature of 30°C. The intensity varies nonlinearly with temperature, with an average sensitivity of 0.045 dB/°C.

The experimental results show that the average bend sensitivity for intensity interrogating are -11.35 dB/m^{-1} and -25.63 dB/m^{-1}. However, the average intensity sensitivity to temperature is 0.045 dB/°C. The intensity sensitivity to bend is much higher than that of temperature. Therefore, the
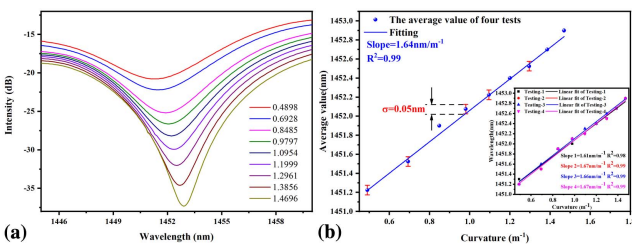

Fig. 7. (a) Interference dip (at 1450 nm) evolution with different curvatures; (b) average wavelength-bending response with error bars for four testing results; the inset shows linear fitting of the four measurements.
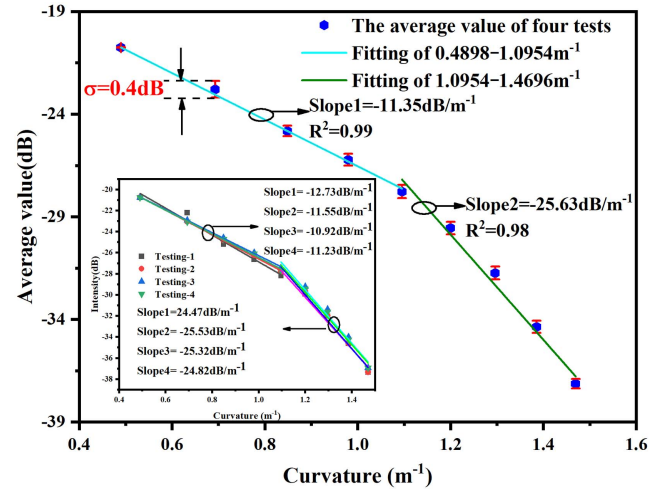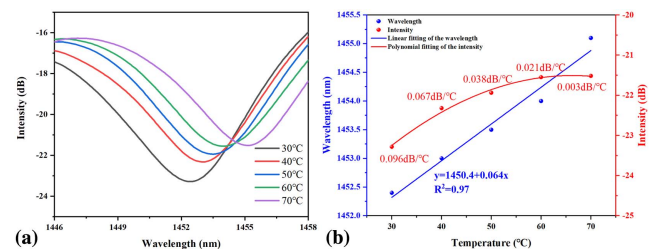

Fig. 9. (a) Spectral responses under different temperatures; (b) wavelength and intensity response to temperature.

Table 1. Performance Comparison between Our Sensors and Other Sensors.

Structure	Sensitivity (dB/m^{-1})	Complexity of Manufacturing Process	Ref.
Helicoidal LPFGs	4.1	Complex	[21]
Superimposed grating	0.6	Complex	[16]
Fiber spindle arrays	−38.4	Moderate	[17]
NCF–SCF–NCF	10.22	Simple	[22]
SMF helical	−7.524	Complex	[18]
Taper–DCF	2.88	Simple	[23]
MMF–RCF–MMF	−25.63	Simple	This work

proposed sensor can use an optical power meter or optical time-domain reflection (OTDR) technology to achieve intensity queries in the case of stable environmental temperature. In the case of significant temperature changes, an OSA can be used to interrogate both wavelength and intensity.

For comparison with the results in the existing literature, some of the reported bending sensors are listed in Table 1. In Ref. [18], these helicoidal long-period fiber gratings are fabricated by twisting SMFs during CO_2 laser irradiation. A compact fiber bending sensor has been presented by superimposing a uniform FBG into a tilted FBG[16]. These gratings are written on hydrogen-carrying germanium-doped SMF by UV laser exposure. Reference [15] reported a bend sensor based on MZI using SMF with a helical structure. The helical structure utilizes an arc-scanning technique to heat an optical fiber rotated at a constant speed of 81 deg/s at one end. Compared to the fabrication methods in Refs. [13,15,18], the literature[14,19,20] and our sensor fabrication require only one commercial SMF fusion splice. The highest sensitivity of −38.4 dB/m^{-1} was reported by Zhang et al.[14]. The sensor consists of four fiber spindles manufactured in manual fusion mode by a fusion splicer. Fabrication of four identical fiber spinners is difficult and requires a high level of operator skill. All fusion splicing in our sensors is done using the automatic fusion mode of commercial SMF fusion splicers. Compared to the 6 cm long sensor reported in Ref. [14], the length of the sensor we provide is only 12 mm. Therefore, we provide a bend sensor that is simple to manufacture, compact, and highly sensitive.

4. Conclusions

In conclusion, a simple and cost-effective bend sensor based on the RCF has been proposed by simply splicing a short segment of RCF with two segments of MMFs. By monitoring the wavelength and intensity changes of the characteristic interference dip (at 1450 nm), the sensor can realize the measurement of bending and temperature. The sensor has a high sensitivity of −25.63 dB/m^{-1} in the range from 1.0954 to 1.4696 m^{-1}.

References

1. H. Gao, D. Xu, Y. Ye, Y. Zhang, J. Shen, and C. Li, "Fiber-tip polymer filled probe for high-sensitivity temperature sensing and polymer refractometers," Opt. Express **30**, 8104 (2022).
2. Z. Zhang, H. Gong, C. Yu, K. Ni, and C. Zhao, "An optical fiber humidity sensor based on femtosecond laser micromachining Fabry-Perot cavity with composite film," Opt. Laser Technol. **150**, 107949 (2022).
3. X. Wang, H. Deng, and L. Yuan, "High sensitivity cascaded helical-core fiber SPR sensors," Chin. Opt. Lett. **19**, 091201 (2021).
4. C. He, C. Zhou, Q. Zhou, S. Xie, M. Xiao, J. Tian, and Y. Yao, "Simultaneous measurement of strain and temperature using Fabry–Pérot interferometry and antiresonant mechanism in a hollow-core fiber," Chin. Opt. Lett. **19**, 041201 (2021).
5. F. Zhang, B. Su, L. Zhong, B. Qi, O. Xu, and Y. Qin, "Ring core few-mode fiber sensor for curvature measurement," Appl. Opt. **61**, 2598 (2022).
6. X. Jin, Z. Rui, Z. Xiang, C. Lu, S. Zhang, X. Xu, M. Lü, Y. Ma, C. Sun, X. Yang, T. Geng, W. Sun, and L. Yuan, "Ultrasensitive liquid level sensor based on slice-shaped composite long period fiber grating," Chin. Opt. Lett. **20**, 011202 (2022).
7. F. Shen, X. Shu, K. Zhou, H. Jiang, H. Xia, K. Xie, and L. Zhang, "Compact vector twist sensor using a small period long period fiber grating inscribed with femtosecond laser," Chin. Opt. Lett. **19**, 090601 (2021).
8. S. Wang, Y. Ma, X. Li, Y. Yi, C. Sun, J. Lin, C. Tong, Y. Li, T. Geng, W. Sun, and L. Yuan, "Highly sensitive torsion sensor based on triangular-prism-shaped long-period fiber gratings," Chin. Opt. Lett. **19**, 041202 (2021).
9. L. Zhu, G. Zhu, A. Wang, L. Wang, J. Ai, S. Chen, C. Du, J. Liu, S. Yu, and J. Wang, "18 km low-crosstalk OAM + WDM transmission with 224 individual channels enabled by a ring-core fiber with large high-order mode group separation," Opt. Lett. **43**, 1890 (2018).
10. X. Li, N. K. Chen, L. Xi, H. Zhang, X. Zhang, W. Zhang, and X. Tang, "Micro-fiber Mach-Zehnder interferometer based on ring-core fiber," Opt. Express **27**, 34603 (2019).
11. Y. Wu, D. Yan, N. K. Chen, K. T. V. Grattan, B. M. A. Rahman, X. Li, Z. Tian, L. Zhang, X. Zhang, X. Zhang, L. Xi, and H. Zhang, "High sensitivity micro-fiber Mach-Zehnder interferometric temperature sensors with a high index ring layer," Opt. Express **27**, 34247 (2019).
12. W. Yuan, Q. Zhao, L. Li, Y. Wang, and C. Yu, "Simultaneous measurement of temperature and curvature using ring-core fiber-based Mach-Zehnder interferometer," Opt. Express **29**, 17915 (2021).
13. W. Yuan and C. Yu, "Dual demodulation of temperature and refractive index using ring core fiber based Mach-Zehnder interferometer," Micromachines **12**, 258 (2021).
14. D. Xiao, G. Wang, F. Yu, S. Liu, W. Xu, L. Shao, C. Wang, H. Fu, S. Fu, P. P. Shum, T. Ye, Z. Song, and W. Wang, "Optical curvature sensor with high resolution based on in-line fiber Mach-Zehnder interferometer and microwave photonic filter," Opt. Express **30**, 5402 (2022).

15. B. Su, F. Zhang, L. Zhong, B. Qi, O. Xu, and Y. Qin, "Temperature compensated curvature sensor with insensitive axial strain based on tapered ring core fiber interferometer," Opt. Commun. **513**, 128067 (2022).

16. X. Dong, Y. Liu, L.-Y. Shao, J. Kang, and C.-L. Zhao, "Temperature-independent fiber bending sensor based on a superimposed grating," IEEE Sens. J. **11**, 3019 (2011).

17. Y. Zhang, Y. Wu, Y. Han, and J. Wu, "The curvature sensor based on fiber-optic spindle arrays," Opt. Laser Technol. **153**, 108153 (2022).

18. X. He, J. Zhou, C. Ma, W. Li, J. Yang, X. Wang, C. Guan, Y. Zhao, and L. Yuan, "Bend sensor based on Mach-Zehnder interferometer using single-mode fiber with helical structure," IEEE Photon. Technol. Lett. **34**, 15 (2022).

19. S. Marrujo-Garcia, I. Hernandez-Romano, M. Torres-Cisneros, D. A. May-Arrioja, V. P. Minkovich, and D. Monzon-Hernandez, "Temperature-independent curvature sensor based on in-fiber Mach-Zehnder interferometer using hollow-core fiber," J. Lightwave Technol. **38**, 1466 (2020).

20. C. Liu, Y. Jiang, B. Du, T. Wang, D. Feng, B. Jiang, and D. Yang, "Strain-insensitive twist and temperature sensor based on seven-core fiber," Sens. Actuator A Phys. **290**, 172 (2019).

21. H. Jung, W. Shin, J. K. Kim, S.-H. Park, D.-K. Ko, J. Lee, and K. Oh, "Bending and strain sensitivities in a helicoidal long-period fiber gratings," IEEE Photon. Technol. Lett. **21**, 1232 (2009).

22. Y. Liu, J. Dong, L. Huang, X. Song, and B. Li, "Investigations on seven-core fiber based interferometric all-fiber sensor for curvature and temperature measurements," Optik **254**, 168638 (2022).

23. F. Wang, L. Zhang, T. Ma, X. Wang, K. Yu, and Y. Liu, "A high-sensitivity sensor based on tapered dispersion compensation fiber for curvature and temperature measurement," Opt. Commun. **481**, 126534 (2021).